Probing the mechanism of inhibition of amyloid-β(1–42)–induced neurotoxicity by the chaperonin GroEL

Marielle A. Wälti[a], Joseph Steiner[b], Fanjie Meng[a], Hoi Sung Chung[a], John M. Louis[a], Rodolfo Ghirlando[c], Vitali Tugarinov[a], Avindra Nath[b], and G. Marius Clore[a,1]

[a]Laboratory of Chemical Physics, National Institute of Diabetes and Digestive and Kidney Diseases, National Institutes of Health, Bethesda, MD 20892-0520; [b]Section of Infections of the Nervous System, National Institute for Neurological Disorders and Stroke, National Institutes of Health, Bethesda, MD 20892; and [c]Laboratory of Molecular Biology, National Institute of Diabetes and Digestive and Kidney Diseases, National Institutes of Health, Bethesda, MD 20892-0530

The human chaperonin Hsp60 is thought to play a role in the progression of Alzheimer's disease by mitigating against intracellular β-amyloid stress. Here, we show that the bacterial homolog GroEL (51% sequence identity) reduces the neurotoxic effects of amyloid-β(1–42) (Aβ42) on human neural stem cell-derived neuronal cultures. To understand the mechanism of GroEL-mediated abrogation of neurotoxicity, we studied the interaction of Aβ42 with GroEL using a variety of biophysical techniques. Aβ42 binds to GroEL as a monomer with a lifetime of ∼1 ms, as determined from global analysis of multiple relaxation-based NMR experiments. Dynamic light scattering demonstrates that GroEL dissolves small amounts of high–molecular-weight polydisperse aggregates present in fresh soluble Aβ42 preparations. The residue-specific transverse relaxation rate profile for GroEL-bound Aβ42 reveals the presence of three anchor-binding regions (residues 16–21, 31–34, and 40–41) located within the hydrophobic GroEL-consensus binding sequences. Single-molecule FRET analysis of Aβ42 binding to GroEL results in no significant change in the FRET efficiency of a doubly labeled Aβ42 construct, indicating that Aβ42 samples a random coil ensemble when bound to GroEL. Finally, GroEL substantially slows down the disappearance of NMR visible Aβ42 species and the appearance of Aβ42 protofibrils and fibrils as monitored by electron and atomic force microscopies. The latter observations correlate with the effect of GroEL on the time course of Aβ42-induced neurotoxicity. These data provide a physical basis for understanding how Hsp60 may serve to slow down the progression of Alzheimer's disease.

amyloid β–chaperonin interactions | NMR spectroscopy | electron microscopy | fluorescence resonance energy transfer | neurotoxicity

Heat shock proteins, also known as chaperones, play a key role in maintaining protein homeostasis and, among other functions, serve to prevent protein misfolding and aggregation (1, 2), thereby protecting cells from a variety of protein misfolding diseases (3–5). Perhaps the most common misfolding disease is Alzheimer's disease, a fatal neurodegenerative condition associated with the accumulation in the brain of amyloid plaques made up of amyloid-β (Aβ) peptides (6).

Random coil Aβ peptides aggregate via multiple oligomeric states into insoluble aggregates and fibrils consisting of a highly ordered cross-β structure (7). Aβ peptides originate from the amyloid precursor protein upon cleavage by β- and γ-secretases, and the most common cleavage products are Aβ(1–40) (Aβ40) and Aβ(1–42) (Aβ42) (8). Of the two peptides, Aβ42 is the more aggregation prone and toxic (9, 10). The exact identity of the toxic species involved in the etiology of Alzheimer's disease is unknown as Aβ aggregation involves many different species appearing simultaneously and transiently (11–13). Aβ peptides are not only located in the extracellular fluid but also aggregate and accumulate in the mitochondrial matrix where they may generate reactive oxygen species that contribute to failure of the energy generation apparatus and consequent neuronal apoptosis (14, 15). Furthermore, in an Alzheimer's disease mouse model,

mitochondrial accumulation of Aβ precedes extracellular fibril formation (16).

There are several families of heat shock proteins (Hsp), named according to their molecular weight. Human Hsp60 is a tetradecameric supramolecular machine (subunit molecular weight, ∼60 kDa) found mainly in the mitochondrial matrix or cytosol, although there is evidence that Hsp60 also plays a functional role extracellularly (17). Hsp60 is evolutionarily highly conserved in terms of sequence, structure, and function (18). Human Hsp60 and its bacterial homolog GroEL share 51% sequence identity and comprise two cylindrical, stacked heptameric rings, each enclosing a large cavity that binds protein substrates (19, 20). Hsp60 alone or in combination with Hsp70 and possibly Hsp90 protects against intracellular β-amyloid stress (21, 22), suggesting a role for Hsp60 in the development of Alzheimer's disease.

Previously, using relaxation-based NMR experiments, we showed that Aβ40 interacts transiently with GroEL (23) via two GroEL-consensus binding sequences (24). Here, we examine the impact of GroEL on Aβ42-induced neuronal cell toxicity and analyze the interaction of Aβ42 with GroEL using a variety of biophysical methods including solution NMR, electron microscopy (EM) and atomic force microscopy (AFM), dynamic light scattering (DLS), and single-molecule fluorescence resonance energy transfer (FRET). We show that GroEL is neuroprotective against the deleterious effects of Aβ42, inhibits the formation of Aβ protofibrils, and slows down Aβ protofibril and fibril formation.

Significance

Chaperones, including the chaperonin Hsp60, facilitate protein folding and prevent protein aggregation, thereby protecting cells from protein misfolding diseases, such as Alzheimer's disease, a fatal neurodegenerative condition associated with the accumulation of amyloid-β plaques in the brain. We show that the bacterial homolog of human Hsp60, GroEL, protects neuronal cell cultures against morphological and electrophysiological damage induced by amyloid-β(1–42). Using a range of biophysical techniques, we demonstrate that transient interactions of GroEL with amyloid-β(1–42) monomers slow down the rate of appearance of protofibrils and fibrils, providing a mechanistic basis for the neuroprotective properties of Hsp60.

Fig. 1. Time course of Aβ42 neuronal toxicity. (*A*) Neuronal cell count over a period of 66 h with medium alone (black), and upon addition of 3 μM Aβ42 in the absence (blue) and presence (red) of 0.7 μM GroEL. Error bars represent 1 SD. (*B*) Electron micrographs of Aβ42 as a function of time. Aβ42 was dissolved in 20 mM sodium phosphate buffer (pH 7.4) to a concentration of 300 μM and left for 3 d at 4 °C; the sample was then diluted to 3 μM (0 h) and incubated (in the absence of GroEL) at 37 °C for a total of 72 h.

Results and Discussion

Aβ42 Neurotoxicity. The neurotoxic concentration range of Aβ42 was established by adding varying concentrations of Aβ42 (0–10 μM) to cell cultures of fluorescently labeled neurons derived from neuronal stem cells and measuring neuronal cell count and neurite length at 72 h postexposure to Aβ42 (*SI Appendix,* Fig. S1*A*). For consistency and reproducibility, Aβ42 was initially dissolved to a concentration of 300 μM, stored at 4 °C for 3 d, and then diluted to the relevant concentration in the cell cultures. A ~50% decrease in both neuronal cell count and mean neurite length was observed at an Aβ42 concentration of 3 μM, which was chosen for all subsequent experiments. GroEL is found to be protective against Aβ42-induced neuronal toxicity in a concentration-dependent manner (*SI Appendix,* Fig. S1*B*): In the absence of GroEL, only ~40% of the neurons survive at 72 h, relative to the control with medium only; addition of 0.07, 0.35, and 0.7 μM GroEL increases neuronal survival to ~58, 61, and 74%, respectively, of the control. All further neuronal cell assays were therefore carried out with 0.7 μM GroEL, which remains stable at 37 °C for at least 6 d (*SI Appendix,* Fig. S2). (Note that 0.7 μM GroEL corresponds to 1.4 μM in substrate binding cavities, 9.8 μM in subunits, and ~0.6 mg/mL of protein; each subunit constitutes a potential binding site, although the occupancy of Aβ42 per cavity is unlikely to exceed 1.)

To further quantitate the extent of Aβ42-induced neurotoxicity and the protective efficacy of GroEL, neuronal cell count was measured over a period 66 h (Fig. 1*A*). For the first 24 h, no evidence of Aβ42-induced neurotoxicity is observed. Thereafter, the neuronal cell count for the Aβ42-treated cell cultures drops rapidly with a half-life of ~24 h, and at 66 h reaches a level of ~30% that of the control (culture medium only). In the presence of GroEL, however, the half-life for the reduction in neuronal cell count is >66 h, at which time the neuronal cell count is reduced to only ~60% of the control. The corresponding electron micrographs of Aβ42, in the absence of GroEL, show that at the start of the experiment the sample consists primarily of protofibrils with a small fraction of fibrils; only after 72 h is the entire sample fibrillized (Fig. 1*B*).

Imaging of neurons containing Td-Tomato fluorescent protein shows that normal morphology is retained for at least 72 h in the absence of Aβ42 (Fig. 2*A, Top* row). In the presence of 3 μM Aβ42, however, disappearance of neurons is clearly apparent at 48 h, and at 72 h no intact neurons remain (Fig. 2*A, Middle* row). The latter changes are significantly reduced upon addition of GroEL (Fig. 2*A, Bottom* row): no morphological changes are observed at 48 h, and only a small amount of neuronal damage is observed at 72 h.

The morphological studies were complemented by electrophysiological analysis using a multielectrode array (MEA) assay monitoring mean firing rate and number of bursts (within a 5-min window). Neuron cultures were monitored for nearly 4 wk, and only after consistent neuronal firing activity in all wells were the neurons exposed to Aβ42 in the absence or presence of GroEL. Neuronal activity was then measured 24 h postexposure. At 24 h postexposure to Aβ42 alone, the mean firing rate and number of bursts is reduced to 30–35% of the levels seen with medium alone; in the presence of GroEL, however, no significant change in either mean firing rate or number of bursts is seen (Fig. 2*B*). The burst duration and the number of spikes per burst are only minimally impacted by Aβ42, with or without GroEL (*SI Appendix,* Fig. S3). The corresponding electron micrographs of the same Aβ42
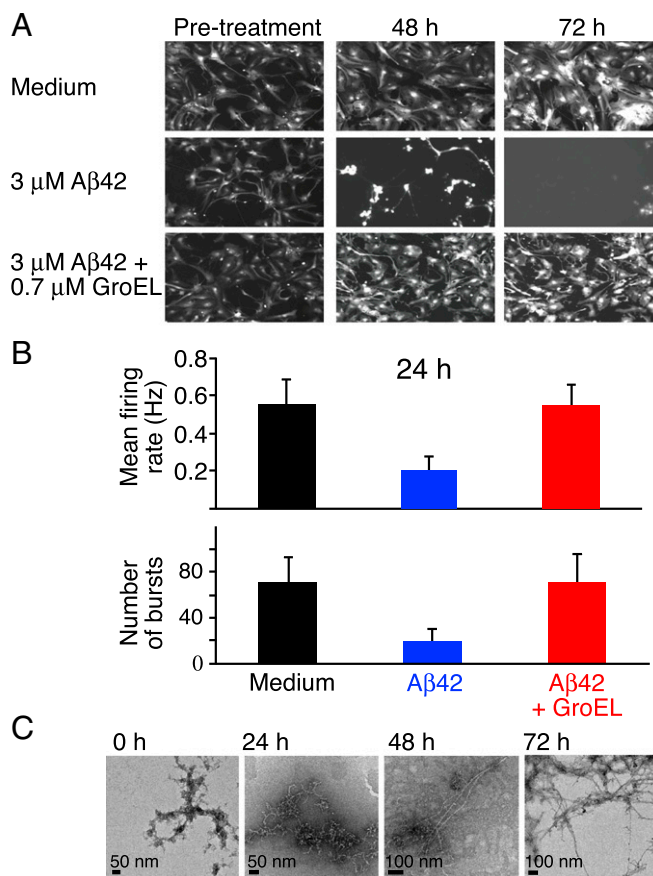
Fig. 2. Images of neuronal cell cultures and electrophysiology. (*A*) Neurons containing the fluorescence label Td-Tomato were imaged at 6-h time intervals. The *Top, Middle,* and *Bottom* rows show some of the images with medium only, 3 μM Aβ42, and 3 μM Aβ42 plus 0.7 μM GroEL, respectively. (Magnification: 10×.) (*B*) Mean firing rate (*Top*) and number of bursts (*Bottom*), measured over a 5-min time frame, of neuronal cell cultures at 24 h for medium only (black), and upon addition of 3 μM Aβ42 in the absence (blue) and presence (red) of 0.7 μM GroEL. Error bars represent 1 SD. (*C*) Corresponding electron micrographs of Aβ42 at various points in time up to 72 h. Aβ42 was dissolved in 20 mM sodium phosphate buffer (pH 7.4) to a concentration of 300 μM and left for 3 d at 4 °C; the sample was then diluted to 3 μM (0 h) and incubated (in the absence of GroEL) at 37 °C for a total of 72 h.

preparation are shown in Fig. 2C: Protofibrils are observed after 24 h at 37 °C, protofibrils and fibrils are seen at 48 h, and at 72 h only fibrils are present.

Initial Interaction of GroEL with Aβ NMR Visible Species. To investigate the mechanism whereby GroEL inhibits Aβ42-induced neurotoxicity, we first measured the overall intensity of the amide proton envelope (from the Fourier transform of the free induction decay of the first t_1 increment of a ^{1}H–^{15}N correlation spectrum) of 100 μM ^{15}N-labeled Aβ42 (Fig. 3A) and Aβ40 (*SI Appendix,* Fig. S4A) within 5 min of addition of unlabeled GroEL (ranging from 0 to 28.6 μM). In both instances, the intensity of the amide proton envelope of the NMR visible Aβ peptides is reduced to ~20–25% of that in the absence of GroEL. As it is difficult to distinguish the free Aβ42 monomer from very small oligomers (such as dimer, trimer, or tetramer), we refer to all of these species as NMR visible species (25).

EM and DLS show that Aβ42, at a concentration of 100 μM, forms oligomeric aggregates immediately after dissolution (within 5 min) at room temperature (Fig. 3 B and C). The amount of Aβ42 aggregates present cannot be determined by DLS since even a very small amount of aggregate leads to significant scattering. The apparent decay time ($t_{1/2}$) of the scattering intensity autocorrelation function for Aβ42 is ~250 μs (Fig. 3C, blue trace). Upon addition of GroEL, the scattering intensity autocorrelation function shifts to a shorter decay time ($t_{1/2}$ ~70 μs; Fig. 3C, red trace), comparable to that observed for GroEL alone ($t_{1/2}$ ~50 μs; Fig. 3C, green trace). These results are reflected in the hydrodynamic radii distribution profiles calculated from the DLS autocorrelation functions (*SI Appendix,* Fig. S5, Top): A small amount of polydisperse high–molecular-weight species (with hydrodynamic radii ranging from 30 to 300 nm) is apparent for Aβ42 alone but disappears upon addition of GroEL, resulting in a major species with a hydrodynamic radius (10.0 ± 0.8 nm) very close to that of GroEL alone (8.7 ± 0.1 nm). Very similar results are

obtained with Aβ40 (*SI Appendix,* Figs. S4B and S5, Bottom). Thus, we conclude from the DLS data that most of the highly scattering oligomers of Aβ40 and Aβ42 are either dissolved into monomers or bound to GroEL without significantly increasing the hydrodynamic radius of the GroEL particles.

To ascertain whether Aβ42 is bound to GroEL as a monomer or in an aggregated state, 100 μM Aβ42 was incubated for a few hours with 7.1 μM GroEL and subjected to electron tomography. No aggregates of Aβ42 can be seen in any of the tomographic slices (*SI Appendix,* Fig. S6A), in contrast to our previous study on another amyloidogenic protein, Het-s, which forms protofibrils upon GroEL binding (26). Further support that the GroEL-binding species of Aβ42 is a monomer is provided by experiments in which Het-s was used to displace bound Aβ42. Previous work demonstrated that Het-s binds to the apical domain of GroEL (26). When 7.1 μM GroEL is added to 100 μM ^{15}N-labeled Aβ42, the intensity of the backbone amide proton envelope of the NMR spectrum of Aβ42 is reduced to about ~60% of that in the absence of GroEL (Fig. 4A); addition of Het-s displaces Aβ42, and, at 150 μM Het-s, the intensity of the backbone amide proton envelope is restored to the level seen in the absence of GroEL (Fig. 4A), indicating that Aβ42 released from GroEL is monomeric (and/or very small NMR visible oligomers). Similar results are observed with Aβ40 (*SI Appendix,* Fig. S4C).

Further confirmation that Aβ42 binds to GroEL as a monomer was obtained using a monomeric fusion construct comprising the GB1 Ig binding domain connected via a linker to the N-terminal end of Aβ42, GB1–Aβ42 (*SI Appendix,* Fig. S7). Addition of 7.1 μM GroEL to 100 μM freshly purified, ^{15}N-labeled GB1–Aβ42 results in a reduction of the backbone amide proton envelope of Aβ42 (which resides between 7.7 and 8.4 ppm, typical of a random coil), while leaving the intensity of the GB1 resonances (arising from a folded globular domain) outside this region unaltered (Fig. 4B).

Kinetics of Aβ42 Binding to GroEL Using Relaxation-Based NMR. The kinetic parameters for the interaction of Aβ42 with GroEL at 5 °C and the dynamics of bound Aβ42, as reported by ^{15}N transverse relaxation rates (^{15}N-R_2^{bound}), were determined from combined analysis of ^{15}N-lifetime line broadening (ΔR_2) (27), dark state exchange saturation transfer (DEST) (28), exchange-induced chemical shifts (29), and Carr–Purcell–Meiboom–Gill (CPMG) relaxation dispersion (30) (Fig. 5). The ^{15}N-ΔR_2 (Fig. 5A) and exchange-induced shift (Fig. 5B) data are not correlated with one another (*SI Appendix,* Fig. S8A), indicating that ΔR_2 arises from lifetime line broadening due to the interaction of the free, NMR visible Aβ42 species with the NMR invisible, GroEL-bound species. The later constitutes a "dark state" owing to its high molecular weight (~800 kDa) and slow tumbling time resulting in very fast transverse relaxation. The ^{15}N-exchange–induced chemical shifts are small but measurable (Fig. 5C), and only residues 19, 20, 41, and 42 show CPMG relaxation dispersions with R_{ex} values of the order of 2 s^{-1} (Fig. 5E). These latter observables, however, serve to decorrelate the bound population (p_B ~1/k_{off} where k_{off} is the dissociation rate constant) from R_2^{bound} when fitted together with the DEST and ΔR_2 data (23).

The results of the global fit of a two-state exchange model (comprising free and bound Aβ42) to the NMR data are shown in Fig. 6. The overall exchange rate between free and bound Aβ42 is ~900 s^{-1} with dissociation (k_{off}) and apparent pseudo–first-order association (k_{app}^{on}) rate constants of 880 ± 70 and 16 ± 1 s^{-1}, respectively; under the conditions of the experiments (50 μM Aβ42 and 2.9 μM GroEL), the GroEL-bound population (p_B) of Aβ42 is ~2%. Assuming the binding of one Aβ42 molecule per GroEL cavity (with two cavities per GroEL) yields a second-order association rate constant k_{on}^{cavity} ~3 × 10^6 M^{-1}·s^{-1} (in terms of GroEL cavities), consistent with diffusion limited binding for molecules of this size, and an equilibrium dissociation constant, K_D^{cavity}, of ~0.3 mM. The latter value is consistent with the results of size
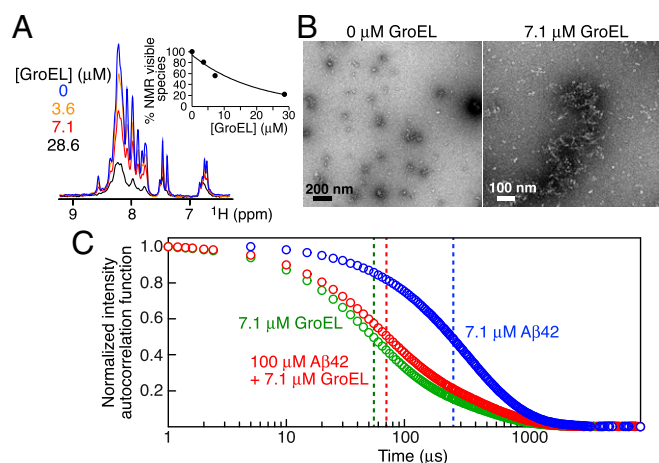
Fig. 3. Interaction of Aβ42 with GroEL during the initial steps of Aβ42 aggregation. (A) Fourier transform of the free induction decay (FID) of the first t_1 increment of a ^{1}H–^{15}N correlation experiment recorded on 100 μM ^{15}N-labeled Aβ42 at 10 °C immediately (time point zero) upon adding 0–28.6 μM GroEL. The Inset shows the overall decrease in the integrated intensity of the backbone amide proton envelope (7.6–8.8 ppm) of the Aβ42 NMR spectrum as a function of GroEL concentration. (B) Electron micrographs of 100 μM Aβ42 in the absence and presence of 7.1 μM GroEL: small aggregates (<200-nm length) of Aβ42 are seen in the absence of GroEL but are undetectable by EM in the presence of GroEL where only GroEL particles are observed. (C) DLS normalized intensity autocorrelation functions ($g^{(2)}$ – 1) obtained immediately after dilution at room temperature (19 °C) of 7.1 μM GroEL (green), 100 μM Aβ42 (blue), and 100 μM Aβ42 plus 7.1 μM GroEL (red). The vertical dashed lines indicate the apparent decay times ($t_{1/2}$).
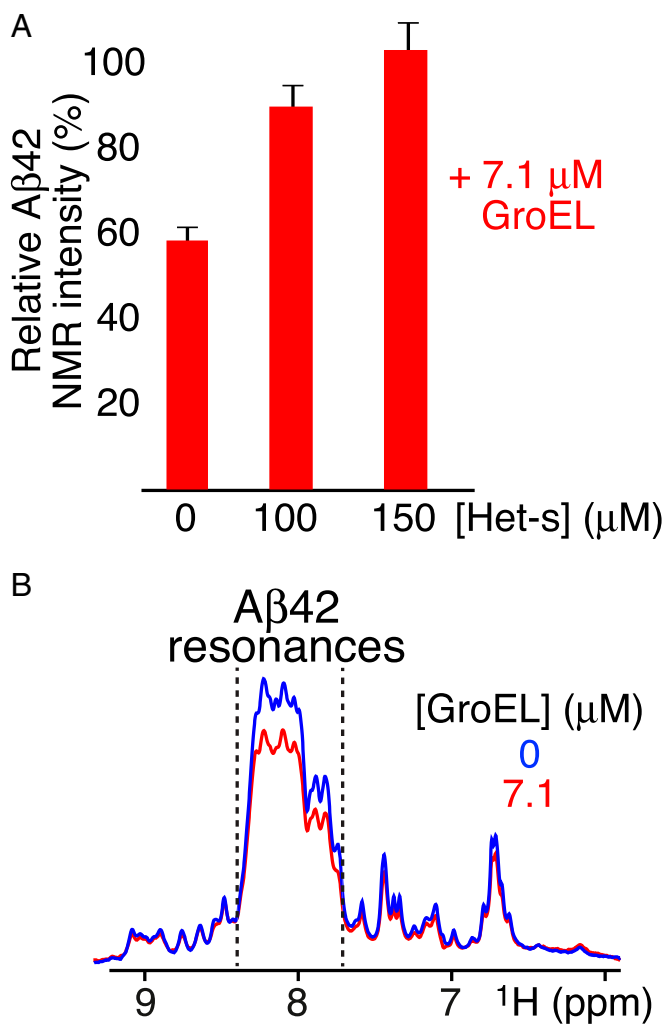
Fig. 4. Effect of addition of Het-s or fusion of Aβ42 with the B1 domain of protein G (GB1) upon GroEL binding. (*A*) Intensity of the backbone amide envelope of 100 μM ^{15}N-labeled Aβ42 immediately after dissolving the peptide (i.e., time point zero) in the presence of GroEL (7.1 μM) relative to that in absence of GroEL. The backbone envelope intensity is obtained from the Fourier transform of the FID of the first t_1 increment of a ^{1}H–^{15}N correlation experiment. Addition of Het-s displaces GroEL-bound Aβ42, resulting in restoration in the intensity of the amide proton envelope of the Aβ42 spectrum to the same level as that seen in the absence of GroEL. (*B*) First Fourier-transformed t_1 increment of a ^{1}H–^{15}N correlation experiment of the ^{15}N-labeled GB1–Aβ42 fusion protein (100 μM, directly after SEC) in the absence (blue) and presence of 7.1 μM GroEL (red). A decrease in intensity of ∼20% is seen between 7.7 and 8.4 ppm (delineated by the dashed lines) which contains all of the backbone amide resonances of Aβ42 (Fig. 3*A*), typical of a random coil, as well as some of GB1, but not downfield of 8.4 ppm or upfield of 7.7 ppm where only Asn and Gln side chain amido (below 7.5 ppm) and GB1 backbone amide resonances (with spectral dispersion characteristic of a folded globular domain) are present, indicating that the fusion protein binds as a monomer and that only the Aβ42 moiety of the fusion protein interacts with GroEL.

exclusion chromatography (SEC) on the GB1–Aβ42 fusion construct, labeled just before the start of the Aβ42 sequence with the fluorophore Alexa 647, carried out in the absence and presence of GroEL (*SI Appendix*, Fig. S9).

The transverse relaxation rate (^{15}N-R_2^{bound}) profile for Aβ42 bound to GroEL, obtained from the global fit, shows the presence of three binding anchor regions comprising residues 16–21, 31–34, and 40–41. These anchor regions are characterized by the largest ^{15}N-R_2^{bound} values and therefore represent the most immo-

bilized regions of Aβ42 when bound to GroEL. The first two regions (residues 16–21 and 31–34) involve the same residues as for the shorter Aβ40 peptide (23) (which only extends up to residue 40), but, in addition, hydrophobic residues close to the C terminus (Val40 and Ile41) of Aβ42 are clearly involved in GroEL binding. In contrast, the last two C-terminal residues of Aβ40 (Val39 and Val40) have low ^{15}N-R_2^{bound} values and are not involved in GroEL binding (23). Moreover, the backbone nitrogen of the C-terminal residue, Ala42, exhibits a significant upfield shift (−1.2 ppm) upon
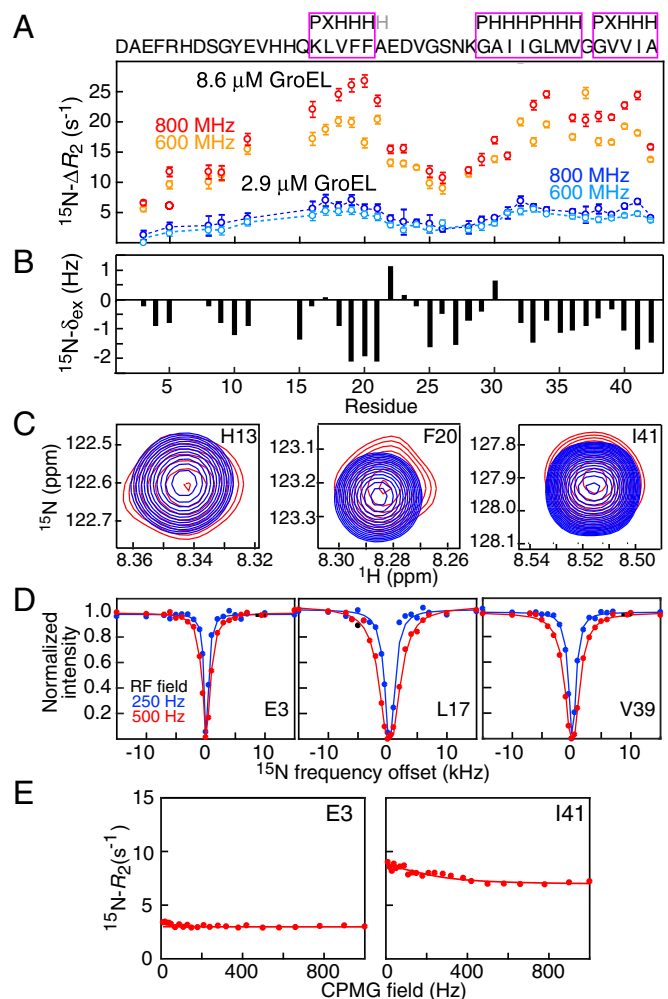
Fig. 5. Relaxation-based NMR experiments probing the interaction of Aβ42 with GroEL at 5 °C. (*A*) ^{15}N lifetime line broadening (^{15}N-ΔR_2) profiles measured on 50 μM ^{15}N-labeled Aβ42 in the presence of 2.9 and 8.6 μM GroEL at two static spectrometer fields (600 and 800 MHz). The sequence of Aβ42 is shown above with the GroEL-binding consensus sequences (24) boxed in magenta (P, polar; H, hydrophobic; X, anything). Open circles are the experimental ΔR_2 data (error bars, 1 SD), and the dashed lines represent the best fits for a two-state exchange model obtained upon globally fitting all of the experimental data (i.e., ^{15}N-ΔR_2, exchange-induced shifts, DEST, and CPMG relaxation dispersion). (*B*) ^{15}N-exchange–induced shifts measured for 50 μM ^{15}N-labeled Aβ42 in the presence of 8.6 μM GroEL at 800 MHz. (*C*) Examples of three ^{1}H–^{15}N cross-peaks of ^{15}N-labeled Aβ42 in the absence (blue) and presence (red) of GroEL. (*D*) Examples of ^{15}N-DEST profiles at two CW RF fields (250 and 500 Hz) of 50 μM ^{15}N-labeled Aβ42 in the presence of 2.9 μM GroEL recorded at a static spectrometer field of 600 MHz. Closed circles are the experimental DEST data, and the solid lines represent the best fits for a two-state exchange model obtained upon globally fitting all experimental data. (*E*) Examples of ^{15}N-CPMG relaxation dispersion curves (with experimental data shown as circles, and best fits by the solid lines) for 50 μM ^{15}N-labeled Aβ42 in the presence of 2.9 μM GroEL recorded at 600 MHz.
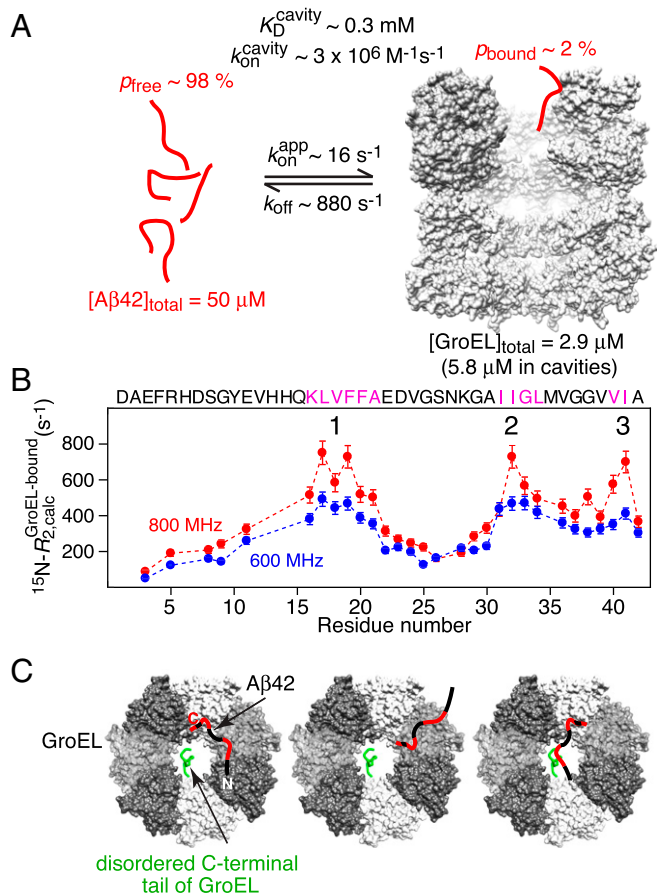
Fig. 6. Results of the analysis of the relaxation-based NMR experiments on the interaction of Aβ42 with GroEL at 5 °C. (*A*) Summary of kinetic parameters obtained upon globally best fitting all NMR relaxation-based data to a two-site exchange model (Fig. 5). Note that the NMR experiments are carried out at equilibrium and analyzed in terms of exchange between two species, free and bound Aβ42; hence k_{on}^{app} is an apparent pseudo–first-order association rate constant in units of per-second that pertains to the specific concentrations of Aβ42 and GroEL used in the NMR experiments. (*B*) ^{15}N-R_2^{bound} profiles for Aβ42 bound to GroEL obtained from the global fits. The three anchor regions (labeled 1–3) for binding to GroEL correspond to residues with the highest ^{15}N-R_2^{bound} values, highlighted by the magenta colored sequences, and lie within the GroEL-binding consensus sequences (Fig. 5*A*). (*C*) Schematic depicting various potential modes of interaction of Aβ42 with GroEL, all of which interconvert on a timescale shorter than the lifetime of the complex (~1 ms). The residues of Aβ42 primarily interacting with GroEL are colored red, the individual subunits of GroEL are shown in different gray scale, and the disordered C-terminal tail of GroEL from one subunit is depicted in green. The spacing between GroEL-binding region 1 and the two other binding regions on Aβ42 is sufficient to permit binding to two adjacent subunits simultaneously; in addition, the disordered glycine/methionine-rich C-terminal tail of GroEL can also potentially make contact with Aβ42.

GroEL binding, as do the backbone nitrogens of residues 17–21, 32–34, and 40–41 (*SI Appendix*, Fig. S8*B*). [Note that the change in ^{15}N shifts of Aβ42 upon binding GroEL are less than 1.5 ppm, consistent with an ensemble of random coil conformations persisting in the bound state (23).] The existence of a third GroEL binding region may account for the ~50% longer lifetime of the GroEL–Aβ42 complex (~1.1 ms) relative to that of the GroEL–Aβ40 complex (~0.7 ms).

As in the case of Aβ40, the maximum ^{15}N-R_2^{bound} values (~700 s^{-1} at 800 MHz) for Aβ42 are 20–25% smaller than the expected value of ~900 s^{-1} (at 800 MHz) if Aβ42 were rigidly bound to a molecule the size of GroEL (~800 kDa). This observation is consistent with

rapid interconversion between different conformational states on a timescale shorter than the lifetime (~1.1 ms) of the complex. Such states likely comprise a mixture of states with one, two, or three contact regions interacting with GroEL at any given time. The separation between region 1 and the other two regions is sufficient to permit Aβ42 to contact two adjacent subunits of GroEL simultaneously. In addition, the methionine/glycine-rich C-terminal disordered tail of GroEL may also transiently contact bound Aβ42, as has been demonstrated using paramagnetic relaxation enhancement measurements for the interaction of a small folded SH3 domain with GroEL (31).

Structural Characterization of Aβ42 Bound to GroEL Using Single-Molecule FRET. Single-molecule FRET of 100 pM Aβ42, labeled with a fluorophore donor (Alexa 488) at the N terminus and a fluorophore acceptor (Alexa 647) at the C terminus (*Experimental Procedures*), is consistent with a broad distribution of rapidly interconverting, disordered conformations (32). We carried out single-molecule FRET measurements on the same Aβ42 construct (at 100 pM) in the presence of GroEL, ranging from 0 to 35.7 μM. GroEL and Aβ42 diffuse freely in solution, and when Aβ42 passes through the confocal beam, a burst of fluorescence is detected.

In the absence of GroEL, Aβ42 has a FRET efficiency of 0.64 (Fig. 7*A*, first panel). Upon addition of 35.7 μM GroEL, the FRET efficiency decreases slightly to 0.62 (Fig. 7*A*, panel 3), indicative of a very small expansion of unfolded Aβ42. That these effects are due to GroEL binding is supported by fluorescence correlation spectroscopy, which shows a reduction in Aβ42 diffusion (manifested by a right shift in the cross-correlation curves) upon addition of GroEL (Fig. 7*B*). To further confirm these observations, 10 nM Aβ42 was incubated with 35.7 μM GroEL and the sample subsequently diluted 100 times to yield a sample comprising 100 pM Aβ42 and 0.36 μM GroEL: The FRET efficiency (Fig. 7*A*, panel 3) increased to 0.67 (Fig. 7*A*, panel 3) and Aβ42 diffusion increased (Fig. 7*B*), close to values observed in the absence of GroEL. Thus, one can conclude that Aβ42 bound to GroEL samples an ensemble of random coil conformations, consistent with previous conclusions, based on backbone chemical shifts, for Aβ40 (23).
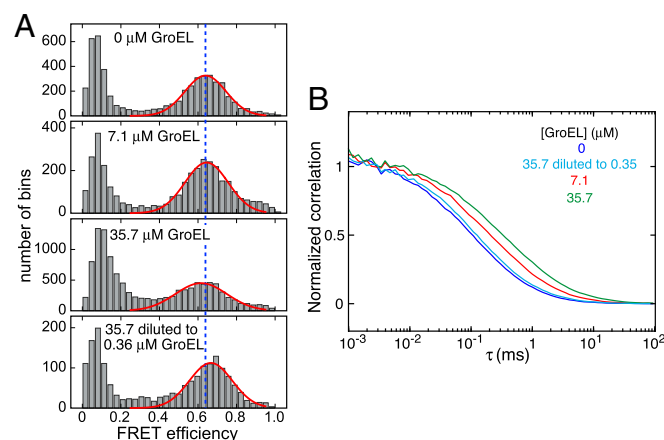
Fig. 7. Probing the interaction of Aβ42 with GroEL by single-molecule FRET. (*A*) FRET efficiency histograms and (*B*) donor–acceptor signal cross-correlation curves recorded on 100 pM Aβ42 labeled with two fluorophores (donor, Alexa 488; acceptor, Alexa 647) in the presence of 0–35.7 μM GroEL. The *Bottom* in *A* and the light blue curve in *B* show the data obtained on a sample of 10 nM Aβ42 incubated with 35.7 μM GroEL and then diluted 100 times to 100 pM Aβ42 and 0.36 μM GroEL. The red solid lines in *A* are the fitted FRET efficiency distributions; the blue dashed line is drawn at a FRET efficiency value of 0.64. All single-molecule FRET experiments were conducted at room temperature (22 °C).

Effect of GroEL on the Progression of Aβ42 Aggregation. The time course of aggregation was followed by monitoring the intensity of the amide proton envelope of the NMR spectrum of ^{15}N-labeled Aβ42 over time (i.e., the disappearance of NMR visible species) (Fig. 8A) and by serial EM (Fig. 8B and *SI Appendix*, S10A) and AFM images (*SI Appendix*, Fig. S10B) in the absence and presence of GroEL (Fig. 8A). In the absence of GroEL, the amide proton envelope intensity decreases rapidly with a $t_{1/2}$ of ~1 d. EM clearly shows that this is due to aggregation (Fig. 8B, *Top*): After 5 h, Aβ42 forms protofibrils, and after 2.5 d at room temperature, fibrillization is complete. In the presence of 3.6–28.6 μM GroEL, there is an initial steep decrease in NMR signal intensity due to binding of the Aβ42 NMR visible species to GroEL followed by a slow decrease (Fig. 8A). The initial phase of the latter is most likely due to the formation of smaller aggregates, which are not observable by either EM or AFM (Fig. 8B, *Lower Left* and *SI Appendix*, Fig. S10). Strikingly, no fibrils were observed in the GroEL-containing samples within the first week (second to fourth rows of *SI Appendix*, Fig. S10 *A and B*), whereas single fibrils can already be seen after 1 d in the absence of GroEL (top row of *SI Appendix*, Fig. S10 *A and B*). In the presence of 3.6 μM GroEL, the first fibrils were observed after 7 d (second row of *SI Appendix*, Fig. S10 *A and B*), with 7.1 μM GroEL between days 7 and 14 (third row of *SI Appendix*, Fig. S10 *A and B*; and Fig. 8B, *Lower Right*), and at 28.6 μM GroEL only after 2 wk (fourth row, *SI Appendix*, Fig. S11 *A and B*). Similarly, GroEL slows down fibril formation for Aβ40: 100 μM Aβ40 is completely fibrillized after 8 d at room temperature in the absence of GroEL but takes 18 d for fibrils to form in presence of 7.1 μM GroEL (*SI Appendix*, Fig. S11). GroEL, however, does not bind as tightly or densely packed to Aβ fibrils (*SI Appendix*, Fig. S12) as it does to Het-s fibrils (26).

Concluding Remarks. We have shown that GroEL, the bacterial homolog of human Hsp60 (55% sequence identity), inhibits Aβ42-induced neurotoxicity, measured both in terms of neuronal morphology and electrophysiology. Using a variety of biophysical techniques, we demonstrate that GroEL binds Aβ42 as a monomer (or other small NMR visible species, perhaps up to a tetramer), slows down the progression of protofibril and fibril formation, and can even dissolve preformed aggregates. The lifetime of the GroEL–Aβ42 complex is on the order of ~1 ms, and while bound, Aβ42 samples a random coil ensemble very similar to that in free solution. The interaction of Aβ42 with GroEL involves three distinct anchor regions, encompassing GroEL-binding consensus sequences (24): residues 16–21, 31–34, and 40–41. The first two regions are shared with Aβ40 (23), but the involvement of the C-terminal residues of Aβ42 is notable as the presence of Ile41 and Ala42 is responsible for Aβ42 being more aggregation prone and neurotoxic than Aβ40 (9, 10). This work therefore suggests that human Hsp60 may play a role in modifying the progression of Alzheimer's disease by reducing the rate of oligomer and protofibril formation and the deposition of Aβ plaques.

Experimental Procedures

Expression and Purification of GroEL. Standard purification of GroEL, including the use of acetone precipitation to remove *Escherichia coli* proteins bound within the two large cavities of GroEL, was carried out as described previously (33). Purified GroEL was stored at a concentration of about 36 μM at 4 °C (all concentrations of GroEL throughout are expressed in terms of the double-ringed full 14-mer, unless stated otherwise). Purity was confirmed by mass spectrometry (MS), SDS/PAGE, and tryptophan fluorescence (34). As GroEL contains no tryptophans, all fluorescence signal can be attributed to protein impurities bound within the GroEL cavities; these protein impurities were always less than 10%. Correct assembly and stability of GroEL was assessed by blue-native–PAGE.

Fig. 8. Time dependence of Aβ42 aggregation in the presence and absence of GroEL. (A) Relative intensity of the backbone amide proton envelope of 50 μM ^{15}N-labeled Aβ42 obtained from the first t_1 increment of a ^{1}H–^{15}N correlation experiment recorded as a function of time (up to 21 d) in the presence of various concentrations of GroEL (ranging from 0 to 28.5 μM). (B) Electron micrographs of Aβ42 over time in the absence (*Top* row) and presence (*Bottom* row) of GroEL. The *Bottom Left* image obtained after 2.5 d in the presence of 28.6 μM GroEL shows no evidence of fibrils; significant fibril formation is apparent in the *Bottom Right* image after 14-d incubation with 7.1 μM GroEL. Serial EM and AFM images over a period of 0–14 d and 0–4 wk, respectively, are shown in *SI Appendix*, Fig. S11. The aggregation was allowed to proceed at room temperature, without shaking.

Expression, Purification, and Sample Preparation of Aβ Peptides. Recombinant, uniformly ^{15}N-labeled Aβ(1–42) (denoted as Aβ42) was either expressed in *E. coli* and purified as previously reported (25) or purchased from rPeptide. Recombinant uniformly ^{15}N-labeled Aβ(1–40) (denoted as Aβ40) was purchased from rPeptide. The purchased Aβ peptides were solubilized in Chelex-treated NaOH and lyophilized as described previously (27). The Aβ peptides were then dissolved in 20 mM sodium phosphate (pH 7.4) and diluted to a concentration of 100 μM (unless specified otherwise). The in-house prepared Aβ42 was prepared as previously reported (25). Briefly, lyophilized Aβ42 was dissolved in 200 μL of 10 mM NaOH and centrifuged for 1 h at 120,000 × g. A volume of 200 μL of 40 mM sodium phosphate (pH 6.9) was added to reach a final pH of 7.4, and the peptide was then diluted with 20 mM sodium phosphate (pH 7.4) to the desired concentration.

Expression and Purification of GB1–Aβ42 Polypeptide. To study a monomeric Aβ42 peptide, a construct was designed where Aβ42 was linked to a soluble model protein GB1 (the first domain of the Ig-binding protein G), which leaves the polypeptide mostly monomeric [>95% by SEC with multiangle

light scattering (SEC-MALS)] for several days at concentrations of around 100 μM, and at a temperature of 4 °C. The DNA insert containing a His$_6$ tag, the GB1 sequence, a factor Xa cleavage site, an Avi-tag, and a cysteine, followed by the Aβ42 sequence (*SI Appendix*, Fig. S7A), was cloned into the pJ414 vector. The ^{15}N-labeled protein was expressed in *E. coli* BL21 in standard minimal media and induced with 1 mM isopropyl β-D-1-thiogalactopyranoside at an optical density at 600 nm of 0.7 for 4 h at 37 °C. The cells were harvested and lysed in buffer A (8 M urea, 50 mM Tris, pH 8.0, and 20 mM imidazole). The lysate was centrifuged at 30,600 × *g* (Dupont Sorval with an SS-34 rotor) for 1 h, and the supernatant was loaded on a 5-mL Ni-NTA column (GE Healthcare) at 3 mL/min. After washing with buffer A, the protein was eluted with buffer A containing 220 mM imidazole at 3 mL/min. The GB1–Aβ42 polypeptide-containing fractions were pooled and applied onto a size exclusion column equilibrated in buffer A at 1.5 mL/min (HiLoad 16/60 Superdex75 column; GE Healthcare; *SI Appendix*, Fig. S8B). The monomeric GB1–Aβ42 polypeptide elutes at ~15 mL. Furthermore, the buffer was exchanged to 20 mM sodium phosphate (pH 7.4) and 25 mM NaCl on an analytical column (Superose 12; 10/300; GE Healthcare) at 0.7 mL/min (*SI Appendix*, Fig. S7 C–E). The purity of the sample was confirmed by SDS/PAGE and mass spectrometry (MS).

Site-Specific Labeling of GB1–Aβ42 Polypeptide. To study small amounts of GB1–Aβ42/GroEL complex by SEC, GB1–Aβ42 was labeled with a fluorescence tag [Alexa Fluor 647 (AL647)]. A volume of 500 μL of GB1–Aβ42 at a concentration of 2.4 mg/mL in 4 M urea and 50 mM Tris·HCl, pH 8.0, was pretreated with 1.5 mM Tris(2-carboxyethyl)phosphine for 2 h before labeling with a fivefold molar excess of AL647 for 2 h. Labeling was confirmed by MS, and excess, unreacted label was removed on a Superose 12 (10/300) column in 20 mM sodium phosphate (pH 7.4) and 25 mM NaCl at 0.5 mL/min.

SEC-MALS. To evaluate the aggregation state of GB1–Aβ42, 250 μg in 125 μL of buffer (20 mM sodium phosphate, pH 7.4, and 25 mM NaCl) was injected onto an analytical size exclusion column (Superose 12; 10/300; GE Healthcare) at a flow rate of 0.5 mL/min. The molecular mass was determined with in-line MALS (DAWN Heleos-II; Wyatt Technology), refractive index (Optilab T-rEX; Wyatt Technology), and UV (Waters 2487; Waters Corporation) detectors. Molecular masses were calculated from the data using the software Astra, version 6.1.

SEC of GB1–Aβ42. A volume of 100 μL of 10 μM Alexa 647-labeled GB1–Aβ42 was loaded onto a Superose 12 (10/300) column equilibrated in 20 mM sodium phosphate (pH 7.4) and 25 mM NaCl at 0.7 mL/min. Elution of the GB1–Aβ42 protein at 15 mL can be visualized by the absorbance at 280 nm or the absorbance of the Alexa Fluor tag at 650 nm. In addition, 0.7 or 2.9 μM GroEL was added to 10 μM Alexa 647-labeled GB1–Aβ42 and also loaded onto the column.

Expression, Purification, and Sample Preparation of Het-s. Het-s(218–289) with a mutation at position 279 (N279A), containing a hexahistidine tag, was purified with a nickel column as described previously (35) and stored as a lyophilized material at ~1 mg per tube at −20 °C. Each tube was dissolved in 200 μL of 45 mM HCl, filtered through a 0.2-μm filter to remove large aggregates, and the pH was adjusted with 1 M Tris (pH 8.0) to a final pH of 7.4 as described in ref. 35. The N279A mutant of Het-s behaves very similarly to wild-type Het-s and forms the exact same fibril structure (35).

Solution-State NMR Spectroscopy and Data Fitting. NMR samples were prepared as described above, and 5% D$_2$O (vol/vol) was added to all samples. Several microliters of the GroEL stock solution were diluted with 20 mM phosphate buffer (pH 7.4) to reach the desired final concentration between 3.6 and 28.6 μM; Aβ peptide was then added to reach a final concentration of 100 μM in a volume of 250 μL. Solution-state NMR experiments were conducted on Bruker 600 and 800 MHz spectrometers equipped with a cryoprobe at 10 °C for aggregation studies and 5 °C for kinetic analysis. All spectra were processed with NMRPipe (36) and analyzed with CCPNMR (37). Standard ^{1}H–^{15}N heteronuclear single quantum correlation (HSQC) spectra were recorded sequentially to study the aggregation kinetics.

^{15}N-R_1 and $R_{1\rho}$ measurements were carried out using previously described pulse sequences (38) at 600 and 800 MHz on samples containing 50 μM ^{15}N-labeled Aβ42 and 0, 2.9, or 8.6 μM GroEL. For the $R_{1\rho}$ measurements, the spin lock periods with a 1-kHz radiofrequency (RF) field strength were applied for 3, 33, 63, 93, 153, and 203 ms. The relaxation delays used for the R_1 measurements were 40, 120, 240, 360, 480, and 640 ms. The R_1 and $R_{1\rho}$ decay curves were fit to a single exponential function, and R_2 values were determined from the relationship $R_2 = (R_{1\rho} - R_1\cos^2\theta)/\sin^2\theta$, where θ is the angle between the effective spin-lock field and the *z* axis of the laboratory frame given by

$\tan^{-1}(\omega_1/\Omega)$, where ω_1 is the spin-lock RF field strength and Ω is the offset of a given resonance from the ^{15}N carrier frequency. Lifetime line-broadening ΔR_2 values are given by the difference in R_2 values obtained in the presence and absence of GroEL.

Two-dimensional ^{15}N-DEST experiments were carried out at 600 MHz on a sample containing 50 μM ^{15}N-labeled Aβ42 and 2.9 μM GroEL, as described previously (28). A ^{15}N continuous-wave (CW) saturation pulse (RF field strength of 250 and 500 Hz) was applied for 0.7 s at 22 different offsets between −15 and 15 kHz from the ^{15}N carrier frequency (located at 118.5 ppm, in the center of Aβ42 spectrum). The reference spectrum was measured with an offset of 15 kHz and a CW RF field of 0 Hz.

The ^{15}N CPMG relaxation dispersion experiments were acquired on a sample containing 50 μM Aβ42 and 2.9 μM GroEL at 600 MHz with ^{1}H$_N$-CW decoupling with a RF field strength of 11 kHz (39). The 10-, 20-, 30-, 40-, 50-, 70-, 90-, 110-, 130-, 150-, 180-, 210-, 240-, 280-, 320-, 380-, 420-, 500-, 580-, 660-, 780-, 900-, and 1,000-Hz CPMG field strengths ($\nu_{CPMG} = 1/2\tau_{CP}$, where τ_{CP} is the delay between CPMG refocusing pulses) were applied for 100 ms.

^{15}N-exchange–induced shifts were measured on ^{15}N-labeled 50 μM Aβ42 from the differences in ^{15}N chemical shifts in the presence and absence of 8.6 μM GroEL at 800 MHz using a standard HSQC experiment. The acquisition time in the indirect ^{15}N dimension was extended using the program SMILE during processing to enhance resolution (40). The measured exchange-induced ^{15}N shifts were scaled down by a factor of 3 to match the ^{15}N-DEST and CPMG relaxation dispersion data acquired in the presence of 2.9 μM GroEL.

The ^{15}N-ΔR_2, DEST, exchange-induced shift, and CPMG relaxation dispersion data were fit globally to a two-state exchange model, numerically solving the McConnell equations (41) as described previously (23).

EM and AFM. Aβ and GroEL samples were prepared in the same manner as described above. Aliquots were taken at different time points and diluted to 5 μM Aβ for AFM measurements, and 1–100 μM Aβ for EM measurements. For EM, 5-μL samples were blotted onto carbon grids (carbon-coated copper grids; Ultrathin Carbon Film/Holey Carbon; Ted Pella) for 1 min, the grids quickly washed with deionized water and further stained with 2% uranyl acetate for 20 s. Images were recorded with a FEI Tecnai T12 electron microscope at 120 kV using a Gatan US1000 CCD camera. For tomograms, tilt series between −60° and +60° in increments of 2° were collected with serial EM (42) using a FEI Tecnai F20 electron microscope operating at 200 kV equipped with a Gatan K2 direct electron detector. The tomograms were reconstructed with the software ETomo routine in the IMOD package (43).

For AFM, 50-μL samples were applied to freshly cleaved mica and incubated for 1 min, washed with 50 μL of deionized water, and air dried. AFM images were taken at a scan rate of 0.7–1 Hz, 256 sampling points per line, and 256 lines in the tapping mode using a MultiMode AFM equipped with a Nanoscope IV controller (Veeco). This included a SPM probe model ACT silicon (Applied Nanostructures) with a 5- to 6-nm tip radius, 40 N/m force constant, and oscillating at ~300 kHz.

Dynamic Light Scattering. Light-scattering experiments were carried out at room temperature (19 °C) on a Brookhaven Instruments Corporation BI-200 goniometer system coupled to a BI-9000 AT autocorrelator and SpectraPhysics Stabilite 2017 argon ion laser operating in the TEM$_{oo}$ mode at 488 nm. A series of intensity autocorrelation functions were collected over 3 min at an angle of 90.0° with delay times set to report on all of the species in solution. Experimental count rates were set to ~500–800 kHz and monitored for stability during data collection. The use of a software dust filter was implemented. Samples of Aβ40 and Aβ42 were studied at a concentration of 100 μM in 20 mM sodium phosphate (pH 7.4) and 25 mM NaCl. Samples of GroEL were studied at a concentration of 7.1 μM in the same buffer in the presence or absence of added Aβ. Data analysis was carried out in real time using the Brookhaven Instruments 9KDLSW 2.12 software package. Data were subsequently analyzed in SEDFIT 15.01c in terms of an intensity-based continuous $I(R_h)$ distribution of hydrodynamic radii of diffusing species with a maximum entropy regularization confidence level of 0.55. Hydrodynamic radii for discrete species were determined by integration of the distribution.

Single-Molecule FRET. Recombinant Aβ42 including two additional amino acids, one nonnatural, 4-acetylphenylalanine (Synchem), at the N terminus and a cysteine at the C terminus was prepared as described previously (32). The two sites were site-specifically labeled by a donor dye (Alexa 488) at the N terminus and an acceptor dye (Alexa 647) at the C terminus. Single-molecule free diffusion experiments were performed using a confocal microscope system (MicroTime200; Picoquant) with a 75-μm-diameter pinhole, a dichroic beamsplitter (ZT405/488/635rpc; Chroma Technology), and an oil-immersion

objective (UPLSAPO; N.A. 1.4, 100×; Olympus). In the free-diffusion experiment, solutions of 100 pM dye-labeled proteins were prepared in 50 mM 1× PBS, pH 7.5. The labeled Aβ42 was incubated with 0, 7.1, 14.3, and 35.7 μM GroEL. The 0.01% Tween 20 (to prevent sticking of proteins on the glass coverslip) and 100 mM β-mercaptoethanol and 40 mM cysteamine (to reduce blinking and bleaching of dyes) were added to the sample. Alexa 488 was excited by a 485-nm diode laser (LDH-D-C-485; PicoQuant) in the CW mode at 20 μW. Alexa 488 and Alexa 647 fluorescence was split into two channels using a beamsplitter (585DCXR; Chroma Technology) and focused through optical filters (ET525/50m for Alexa 488 and E600LP for Alexa 647; Chroma Technology) onto photon-counting avalanche photodiodes (SPCM-AQR-16; PerkinElmer Optoelectronics). Photons were collected into 2-ms bins for 1–2 h, and those containing 40 photons or more were considered as significant bursts for further analysis. All binned bursts were subject to a FRET efficiency versus bursts number plot and fluorescence correlation spectroscopy analysis. All experiments were performed at room temperature (22 °C). Additional details of the single-molecule FRET experiments and the fitting procedures have been described elsewhere (44–46).

Human Neural Stem Cell-Derived Neuronal Cultures. Human neural stem cell (NSC)-derived neuronal cultures were prepared as described previously (47). Briefly, NSCs were split into a 96-well plate coated with 0.002% poly-L-ornithine (Sigma) and 10 μg/mL laminin (Life Technologies) at 7,500–10,000 cells per cm², and neuronal differentiation medium was added 24 h after plating. The differentiation medium contained DMEM/F12 with GlutaMax, 1.8% BSA, 1× StemPro hESC supplement (all from Life Technologies), 10 ng/mL BDNF, and glial cell line-derived neurotrophic factor (R&D Systems), and cells received fresh medium and growth factors every other day. Neurons at day 7–12 in vitro were utilized in neurotoxicity assays.

Aβ Neurotoxicity Experiments. Human neuronal cultures (15–20,000 cells per well), stably expressing Td-Tomato fluorescent protein to label the cells and processes, were plated onto 96-well plates as described above and were maintained at 37 °C in a humidified tissue culture incubator at 5% CO₂. Neuronal cultures were treated with differentiation media as described above and with GroEL at a final concentration of 0.7 μM. After 60-min

preincubation, Aβ42 (rPeptide) was added to a final concentration of 3 μM. The neuronal cultures were observed with a GE INCell Analyzer 2000 BioImager to acquire images of each well (four images per well) at various time points, 24, 48, and 72 h posttreatment. High content imaging/analysis of these cultures was achieved with GE Investigator 1.93 analysis software. Neuronal viability, neurite length, and other morphological parameters were quantitated for each sample. Time-lapse experiments were conducted with the BioTek Cytation 5/BioSpa imager or the NanoEntek JuLI Stage imagers, with images being captured every 6 h for 4 d. These data were analyzed with MetaMorph Premier software, Version 7.8.13.0 (Molecular Devices). The data were depicted with GraphPad Prism 7.02.

Electrophysiological Analysis with Axion Maestro MEA Assays. Forty-eight-well t-MEA plates were utilized to plate the human neuronal cultures for analysis. These plates contain 16 active recording electrodes per well. A total of 200,000 neurons was applied to each well of the t-MEA plate, and cultures were maintained at 37 °C in a humidified tissue culture incubator at 5% CO₂. Electrophysiological activity, noted by increased spike rate in the wells, increased significantly by 21 d in vitro and was monitored by recording spontaneous electrical activity in all wells for 5 min per day. At this point, the human neuronal cultures were treated with differentiation media (described above) and with 0.7 μM GroEL. After 60-min preincubation, Aβ42 was added to a final concentration of 3 μM. Spontaneous electrical activity was recorded daily afterward, beginning at 24 h posttreatment. Quantitation of electrical activity was carried out with Axion Axis software. Parameters such as number of spikes, mean firing rate, and number of bursts were determined for each treatment.

1. Balch WE, Morimoto RI, Dillin A, Kelly JW (2008) Adapting proteostasis for disease intervention. *Science* 319:916–919.
2. Hartl FU, Bracher A, Hayer-Hartl M (2011) Molecular chaperones in protein folding and proteostasis. *Nature* 475:324–332.
3. Muchowski PJ, Wacker JL (2005) Modulation of neurodegeneration by molecular chaperones. *Nat Rev Neurosci* 6:11–22.
4. Zhang H, Xu LQ, Perrett S (2011) Studying the effects of chaperones on amyloid fibril formation. *Methods* 53:285–294.
5. Arosio P, et al. (2016) Kinetic analysis reveals the diversity of microscopic mechanisms through which molecular chaperones suppress amyloid formation. *Nat Commun* 7: 10948.
6. Masters CL, et al. (1985) Amyloid plaque core protein in Alzheimer disease and Down syndrome. *Proc Natl Acad Sci USA* 82:4245–4249.
7. Greenwald J, Riek R (2010) Biology of amyloid: Structure, function, and regulation. *Structure* 18:1244–1260.
8. Costanzo M, Zurzolo C (2013) The cell biology of prion-like spread of protein aggregates: Mechanisms and implication in neurodegeneration. *Biochem J* 452:1–17.
9. Jarrett JT, Berger EP, Lansbury PT, Jr (1993) The carboxy terminus of the β amyloid protein is critical for the seeding of amyloid formation: Implications for the pathogenesis of Alzheimer's disease. *Biochemistry* 32:4693–4697.
10. El-Agnaf OM, Mahil DS, Patel BP, Austen BM (2000) Oligomerization and toxicity of β-amyloid-42 implicated in Alzheimer's disease. *Biochem Biophys Res Commun* 273: 1003–1007.
11. Bucciantini M, et al. (2002) Inherent toxicity of aggregates implies a common mechanism for protein misfolding diseases. *Nature* 416:507–511.
12. Walsh DM, et al. (2002) Naturally secreted oligomers of amyloid β protein potently inhibit hippocampal long-term potentiation in vivo. *Nature* 416:535–539.
13. Selkoe DJ (2003) Folding proteins in fatal ways. *Nature* 426:900–904.
14. Chen JX, Yan SD (2007) Amyloid-beta-induced mitochondrial dysfunction. *J Alzheimers Dis* 12:177–184.
15. Han XJ, et al. (2017) Amyloid β-42 induces neuronal apoptosis by targeting mitochondria. *Mol Med Rep* 16:4521–4528.
16. Du H, et al. (2010) Early deficits in synaptic mitochondria in an Alzheimer's disease mouse model. *Proc Natl Acad Sci USA* 107:18670–18675.
17. Pei W, et al. (2016) Extracellular HSP60 triggers tissue regeneration and wound healing by regulating inflammation and cell proliferation. *NPJ Regen Med* 1:16013.
18. Zeilstra-Ryalls J, Fayet O, Georgopoulos C (1991) The universally conserved GroE (Hsp60) chaperonins. *Annu Rev Microbiol* 45:301–325.
19. Thirumalai D, Lorimer GH (2001) Chaperonin-mediated protein folding. *Annu Rev Biophys Biomol Struct* 30:245–269.
20. Nisemblat S, Yaniv O, Parnas A, Frolow F, Azem A (2015) Crystal structure of the human mitochondrial chaperonin symmetrical football complex. *Proc Natl Acad Sci USA* 112:6044–6049.
21. Veereshwarayya V, Kumar P, Rosen KM, Mestril R, Querfurth HW (2006) Differential effects of mitochondrial heat shock protein 60 and related molecular chaperones to prevent intracellular beta-amyloid-induced inhibition of complex IV and limit apoptosis. *J Biol Chem* 281:29468–29478.
22. Jebara F, Weiss C, Azem A (September 15, 2017) Hsp60 and Hsp70 chaperones: Guardians of mitochondrial proteostasis. *eLS*, 10.1002/9780470015902.a002/152.
23. Libich DS, Fawzi NL, Ying J, Clore GM (2013) Probing the transient dark state of substrate binding to GroEL by relaxation-based solution NMR. *Proc Natl Acad Sci USA* 110:11361–11366.
24. Stan G, Brooks BR, Lorimer GH, Thirumalai D (2006) Residues in substrate proteins that interact with GroEL in the capture process are buried in the native state. *Proc Natl Acad Sci USA* 103:4433–4438.
25. Wälti MA, Orts J, Vögeli B, Campioni S, Riek R (2015) Solution NMR studies of recombinant Aβ(1–42): From the presence of a micellar entity to residual β-sheet structure in the soluble species. *ChemBioChem* 16:659–669.
26. Wälti MA, et al. (2017) Chaperonin GroEL accelerates protofibril formation and decorates fibrils of the Het-s prion protein. *Proc Natl Acad Sci USA* 114:9104–9109.
27. Fawzi NL, Ying J, Torchia DA, Clore GM (2010) Kinetics of amyloid β monomer-to-oligomer exchange by NMR relaxation. *J Am Chem Soc* 132:9948–9951.
28. Fawzi NL, Ying J, Ghirlando R, Torchia DA, Clore GM (2011) Atomic-resolution dynamics on the surface of amyloid-β protofibrils probed by solution NMR. *Nature* 480: 268–272.
29. Skrynnikov NR, Dahlquist FW, Kay LE (2002) Reconstructing NMR spectra of "invisible" excited protein states using HSQC and HMQC experiments. *J Am Chem Soc* 124:12352–12360.
30. Palmer AG, 3rd, Kroenke CD, Loria JP (2001) Nuclear magnetic resonance methods for quantifying microsecond-to-millisecond motions in biological macromolecules. *Methods Enzymol* 339:204–238.
31. Wälti MA, Libich DS, Clore GM (2018) Extensive sampling of the cavity of the GroEL nanomachine by protein substrates probed by paramagnetic relaxation enhancement. *J Phys Chem Lett* 9:3368–3371.
32. Meng F, et al. (2018) Highly disordered amyloid-β monomer probed by single-molecule FRET and MD simulation. *Biophys J* 114:870–884.
33. Grason JP, Gresham JS, Widjaja L, Wehri SC, Lorimer GH (2008) Setting the chaperonin timer: The effects of K⁺ and substrate protein on ATP hydrolysis. *Proc Natl Acad Sci USA* 105:17334–17338.
34. Todd MJ, Lorimer GH (1998) Criteria for assessing the purity and quality of GroEL. *Methods Enzymol* 290:135–141.

35. Daskalov A, et al. (2014) Contribution of specific residues of the β-solenoid fold to HET-s prion function, amyloid structure and stability. *PLoS Pathog* 10:e1004158.

36. Delaglio F, et al. (1995) NMRPipe: A multidimensional spectral processing system based on UNIX pipes. *J Biomol NMR* 6:277–293.

37. Vranken WF, et al. (2005) The CCPN data model for NMR spectroscopy: Development of a software pipeline. *Proteins* 59:687–696.

38. Lakomek NA, Ying J, Bax A (2012) Measurement of ^{15}N relaxation rates in perdeuterated proteins by TROSY-based methods. *J Biomol NMR* 53:209–221.

39. Hansen DF, Vallurupalli P, Kay LE (2008) An improved ^{15}N relaxation dispersion experiment for the measurement of millisecond time-scale dynamics in proteins. *J Phys Chem B* 112:5898–5904.

40. Ying J, Delaglio F, Torchia DA, Bax A (2017) Sparse multidimensional iterative lineshape-enhanced (SMILE) reconstruction of both non-uniformly sampled and conventional NMR data. *J Biomol NMR* 68:101–118.

41. McConnell HM (1958) Reaction rates by nuclear magnetic resonance. *J Chem Phys* 28:430–431.

42. Mastronarde DN (2005) Automated electron microscope tomography using robust prediction of specimen movements. *J Struct Biol* 152:36–51.

43. Kremer JR, Mastronarde DN, McIntosh JR (1996) Computer visualization of three-dimensional image data using IMOD. *J Struct Biol* 116:71–76.

44. Chung HS, Louis JM, Eaton WA (2009) Experimental determination of upper bound for transition path times in protein folding from single-molecule photon-by-photon trajectories. *Proc Natl Acad Sci USA* 106:11837–11844.

45. Merchant KA, Best RB, Louis JM, Gopich IV, Eaton WA (2007) Characterizing the unfolded states of proteins using single-molecule FRET spectroscopy and molecular simulations. *Proc Natl Acad Sci USA* 104:1528–1533.

46. Chung HS, et al. (2017) Oligomerization of the tetramerization domain of p53 probed by two- and three-color single-molecule FRET. *Proc Natl Acad Sci USA* 114:E6812–E6821.

47. Efthymiou A, et al. (2014) Functional screening assays with neurons generated from pluripotent stem cell-derived neural stem cells. *J Biomol Screen* 19:32–43.